THE EFFECT OF ENTRANCE CONDITIONS ON TURBULENT SWIRLING JETS AT LOW RE-NUMBERS

Wolfgang Kollmann
MAE Department,
University of California Davis
Davis, CA 95616, USA
wkollmann@ucdavis.edu

ABSTRACT

The turbulent flow in swirling jets with swirl number large enough for vortex breakdown is investigated numerically. Three variants for the entrance boundary conditions and disturbances are simulated starting from stagnant initial conditions. The formation of the recirculation zone and the associated vortical structures are documented and compared to flow visualisations.

INTRODUCTION

Swirling flows are of importance for theoretical and practical reasons (Leibovich, (1978)): They are subject to competing instability mechanisms and are able to generate a rich variety of flow structures, which are not completely understood (Serre and Bontoux (2002), Ruith et al. (2003), Kurosaka et al. (2006)), and swirling jets at sufficiently high swirl numbers form a recirculation zones that have important practical applications. Swirling jet flows at moderate Reynolds and high swirl numbers are investigated using direct numerical simulations to examine the role of the entrance boundary conditions and associated disturbances.

NUMERICAL METHOD

A hybrid spectral-finite difference method (Kollmann and Roy (2000), Kollmann (2007)) is used to solve the incompressible Navier-Stokes equations in cylindrical coordinates in flow domains that can be mapped smoothly onto the cylinder with radius unity. The discrete Fourier transform $\mathcal{F}_N$ (FFT)

$$\varphi(\theta_j) = \mathcal{F}_N^{-1}(\tilde{\varphi}(k)), \quad \tilde{\varphi}(k) = \mathcal{F}_N(\varphi(\theta_j)) \tag{1}$$

where $\theta_j = 2\pi j/N$ are the discrete azimuthal collocation points, is then applicable to the azimuthal direction in the image domain and the Navier-Stokes equations emerge as pdes for complex-valued Fourier modes. The system of mode equations consists of two $N/2+1$-sets for transport variables and two $N/2 + 1$-sets for elliptic variables. The transport variables are the azimuthal velocity modes $\tilde{v}_\theta(k, r, z, t)$ and the vorticity mode combination $\tilde{W}(k, r, z, t)$ defined by

$$\tilde{W} \equiv \tilde{\Omega}_\theta - iH(k)\tilde{\Omega}_r \tag{2}$$

where $k = 0, \cdots, N/2$ is the azimuthal wavenumber, $H(0) = 0$ and $H(k) = 1$ for $k \neq 0$, and $\tilde{\Omega}_\theta$, $\tilde{\Omega}_r$ denote the azimuthal and radial vorticity components. The pdes for these variables can be found in Kollmann (2007).

The first set of elliptic variables is constructed by observing, that mass balance can be eliminated, since it can be cast in the form

$$\frac{\partial}{\partial r}[r(\tilde{v}_r + ik\langle\tilde{v}_\theta\rangle)] + \frac{\partial}{\partial z}(r\tilde{v}_z) = 0 \tag{3}$$

where the angular brackets indicate radial averaging

$$\langle\tilde{v}_\theta\rangle \equiv \frac{1}{r}\int_0^r dr'\,\tilde{v}_\theta(k, r', z, t) \tag{4}$$

It follows from this pde that a complex-valued streamfunction exists for each azimuthal wavenumber k such that

$$d[r\tilde{\Psi}(r, k, z, t)] = -r\tilde{v}_z dr + r(\tilde{v}_r + ik\langle\tilde{v}_\theta\rangle)dz \tag{5}$$

is exact and the radial and axial velocity components can be recovered by

$$-r\tilde{v}_z = \frac{\partial}{\partial r}(r\tilde{\Psi})$$

$$\tilde{v}_r = -ik\langle\tilde{v}_\theta\rangle + \frac{\partial\tilde{\Psi}}{\partial z} \tag{6}$$

The streamfunction modes $\tilde{\Psi}(k, r, z, t)$, $k = 0, \cdots, N/2$ are then governed by

$$\frac{\partial}{\partial r}\left(\frac{1}{r}\frac{\partial}{\partial r}(r\tilde{\Psi})\right) - \frac{k}{r^2}\frac{\partial}{\partial r}(r\tilde{\Psi}) + \frac{\partial^2\tilde{\Psi}}{\partial z^2} =$$

$$i\frac{\partial}{\partial z}(k\langle\tilde{v}_\theta\rangle - H(k)\tilde{v}_\theta) + \tilde{W} \tag{7}$$

The right side indicates the appropriate choice $\tilde{v}_\theta$, $\tilde{W}$ for the transport variables. The streamfunction modes are the solutions of the Helmholtz pdes, that can be shown to insure mass balance and satisfy the pole conditions (Boyd (2001), Constantinesu and Lele (2002), Kollmann (2007)) for all Fourier modes due to the particular wavenumber dependence of the differential operator.

The second set of elliptic variables are the pressure modes $\tilde{P}(k, r, z, t)$ for $k = 1, \cdots, N/2$. They are the solutions of elliptic pdes that follow from mass amd momentum balances, details are given in Kollmann (2007). The pressure solutions can be shown to satisfy all pole conditions.

The transport pdes are discretized using central difference operators with accuracy from 2nd to 8th at inner points and 3rd order one-sided schemes near boundaries. The convective terms are discretized using upwind-biased schemes of order 3 to 9, the solver allows the selection of central differences with explicit numerical filters, strictly upwind-biased schemes or skew-symmetric formulation. The latter is applied in the present simulations ($\alpha = 0.5$), it is given by

$$A_i(\mathbf{v}, \mathbf{f}) = \alpha T_i(\mathbf{v}, \mathbf{f}) + (1 - \alpha)\hat{T}_i(\mathbf{v}, \mathbf{f}) \tag{8}$$

where **f** is a vector field and T_i and $\hat{T}_i$, $i = r, \theta, z$ denote the non-conservative and conservative forms of the convective part of the time rate of change following a material point. The time integrator is an explicit 4th-order, 5-stage, state space Runge-Kutta method (Hairer and Wanner (1996)).

Numerical parameters

The flow domain is the cylinder $(\theta, r, z) \in \mathcal{D} = [0, 2\pi] \times [0, 5.5D] \times [0, 10D]$ designed for the investigation of the near field of vortex breakdown. The simulations used the skew-symmetric form (8) of the convective terms with either the 5th (case III) or 9th (cases I and II) order for the upwind-biased part and the 4th (case III) or 8th (cases I and II) order central finite-difference operators, $N = 128$ azimuthal Fourier modes and $n_r = 91$, $n_z = 175$ grid points in the radial and axial directions. The resolution in azimuthal direction required for uniform discretization in radial direction increases linearly with r, hence N should be a linear function of r with $N(0) = 5$. This is achieved by increasing N blockwise with r such that N is a power of two. The Poisson equations for the streamfunction and pressure modes are solved with an iterative method using deferred corrections and LU-decomposition of the coefficient matrix. The deferred corrections method is designed to reduce the bandwidth of the coefficient matrix.

Boundary conditions

The velocity components are prescribed at the entrance boundary $\tilde{v}_r^b(k, r, t)$, $\tilde{v}_\theta^b(k, r, t)$, $\tilde{v}_z^b(k, r, t)$ and the conditions for the transport and elliptic variables can be deduced from the relations to velocity. For the streamfunction modes $\tilde{\Psi}$ at the boundary are given as Dirichlet conditions according to (), (4)

$$\tilde{\Psi}^b(k, r, t) = -\langle r\tilde{v}_z^b\rangle(k, r, t) \qquad (9)$$

The azimuthal velocity modes are specified directly $\tilde{v}(k, r, 0, t) = \tilde{v}_\theta^b(k, r, t)$. The mode combination $\tilde{W}$ is given at the boundary by (2)

$$\tilde{W}^b = \frac{\partial}{\partial z}(\tilde{v}_r + iH\tilde{v}_\theta) - r^k \frac{\partial}{\partial r}\left(\frac{\tilde{v}_z^b}{r^k}\right) \qquad (10)$$

The pressure modes for $k = 1, \cdots, N/2$ are Dirichlet conditions following from the transport pde for $\tilde{v}_\theta$

$$\tilde{P}(k, r, t) = \frac{i\rho r}{k}\left(\frac{\partial \tilde{v}_\theta^b}{\partial t} + T_\theta - \frac{1}{Re}F_\theta\right) \qquad (11)$$

where T_θ denotes the convective and F_θ the viscous terms. At the exit boundary convective conditions for $\tilde{v}_\theta$ and $\tilde{W}$ are prescribed and the streamfunction $\tilde{\Psi}$ and pressure $\tilde{p}$ modes satisfy zero gradient conditions. At the upper boundary Dirichlet conditions are used. The axis $r = 0$ is not boundary, but kinematic conditions following from the pole conditions are prescribed.

RESULTS

Three sets of simulation results are presented:

Case I: The swirling jet flow of Billant et al. (1998) for the Reynolds number $Re = 1000$ and the swirl number $S^* = 1.4$.

Case II: The flow of Liang and Maxworthy (2005) for the Reynolds number $Re = 1000$ and the swirl number $S = 1.1$ with disturbances in the flow field near the entrance section.

Case III: The flow of Liang and Maxworthy (2005) for the same Reynolds and swirl numbers as case II but without disturbances in the flow field.

The disturbances in the flow field for cases I and II were generated by application of a low-pass filter (azimuthal amplitudes for $k > 64$ are damped out) in the meridional subdomain $0 \le r \le 5.5, 0 \le z \le 0.2$ to the increments of the solution.

Simulation conditions

All simulations were started from stagnant conditions with the axial velocity at the entrance smoothly ramped up within $\triangle t = 2.0$ and the azimuthal velocity in $\triangle t = 4.0$ (dimensionless) time units to the asymptotic profiles. Disturbances were added to the basic entrance profiles for the azimuthal wavenumbers $k > 0$ and frequency of order $\omega = 0.2$ with amplitudes less than 1% to break the symmetry of the solution. The simulation conditions were chosen as $Re = 10^3$ and the swirl numbers $S = 1.1$ as defined by Liang & Maxworthy (2005)

$$S \equiv \frac{\Omega D}{2v_z(0,0)} \qquad (12)$$

where Ω is the rotation rate of the entrance pipe and $v_z(0,0)$ the axial velocity at the entrance, for cases II and III, and $S^* = 1.4$ as defined in Billant et al. (1998)

$$S^* \equiv \frac{2v_\theta(R/2, z_0)}{v_z(0, z_0)} \qquad (13)$$

where $z_0 = 0.4D$, $D = 2R$ being the nozzle diameter, for case I. The entrance profiles in fig.1 for the Liang & Maxworthy (2005) flow (lower graph) were generated by rotating the jet pipe, whereas the profiles for the Billant et al. flow (1998) are generated by upstream vanes. The vanes create the bulge in the entrance profile proportional to the swirl number, the profile shown in fig.1 corresponds to the asymptotic value of the swirl number. The difference in these profiles is the overlap of azimuthal and axial profiles in the outer region near $r/D = 0.5$.
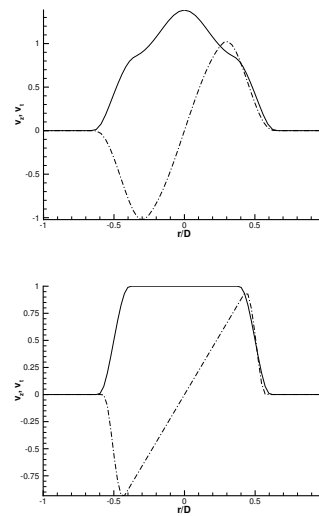

Figure 1: Entrance profiles for $v_z(r)$ (full lines) and $v_\theta(r)$ (dot-dashed lines) for the Billant et al. flow (1998) (upper graph) and the Liang and Maxworthy (2005) flow (lower graph).

Results for Case I

The results for the Billant et al. (1998) flow in fig.2 and fig.3 show that the Kelvin-Helmholtz instability is dominant in the outer boundary layer leading first to the formation of the conical, counterrotating shear layer and then to its break-up into spiral, counter-rotating vortex tubes. The
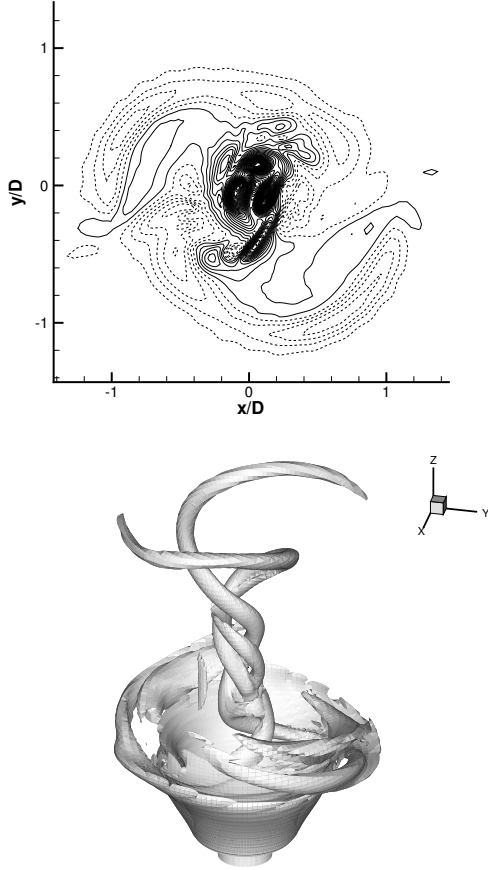

Figure 2: Vorticity component Ω_z at $z/D = 2.14$ (upper graph, full lines are positive and dashed lines negative values, max $|\Omega_z| = 16.99$) and the level surface for enstrophy Ω_θ (lower graph, $|\Omega| = 6.082$, max $|\Omega| = 22.52$) for $Re = 1000$, $S^* = 1.4$ at $t = 15.98$ for the Billant et al. (1998) flow.

formation of the recirculation zone is observed at $t = 4.91$. The initial phase of the breakdown is dominated by the convection of rotating fluid towards the axis in the wake of the first vortex ring. Stretching leads to rapid increase in axial vorticity and the formation of three helical vortex tubes as is evident in fig.2. The three tubes have positive axial vorticity, hence induce rotational motion on each other. The interaction with the surrounding vorticity with opposite sense of rotation distorts the tubes quickly and they become part of the turbulent flow in the recirculation bubble as can be seen in fig.3 showing enstrophy in the upper and the isolines of Ω_θ in a meridional plane in the lower graph at $t = 17.12$.

Results for case II

The results for the Liang & Maxworthy flow (case II, with disturbances near the entrance section) in fig.4 and fig.5 show for $0 \leq z/D < 1.6$ the development of vortex rings in the outer boundary layer that are interacting with the left wall boundary and the outer flow, the dominant azimuthal
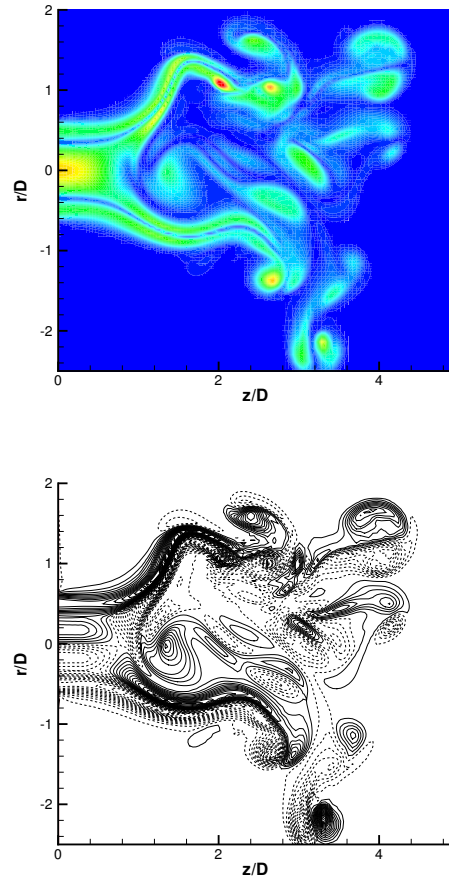

Figure 3: Enstrophy (upper graph, max $|\Omega| = 13.83$, range shown is $[0, 12]$ with red indicating the highest value) and Ω_θ (lower graph, full lines are positive and dashed lines negative values) for $Re = 1000$, $S^* = 1.4$ at $t = 17.12$ for the Billant et al. (1998).

wavenumber in this region is $k = 5$. The interaction with the wall boundary produces the vortex loops visible near the left side of the lower graph in fig.4. The presence of longitudinal/spiral vortices is evident in the cross-sectional plots in fig. 5. The upper graph showing the isolines of the axial velocity and the lower graph the vorticity combination W demonstrate the dominance of the azimuthal wavenumber range $k = 4 \rightarrow 6$ in the outer shear layer. The vortex breakdown is observed at $t = 6.26$.

Results for case III

The only difference between case III and case II is the absence of the low pass filter near the entrance section, all other parameters are the same. The absence of these disturbances precludes the development of the instability of the outer part of the conical shear layer. The evolution of the flow shows the emergence of the conical jet as in case I for the conditions of the Billant et al. (1998) experiment. However, the azimuthal wavenumber $k = 1$ becomes dominant and a radial, flapping motion ensues as can be seen in fig.6. This motion folds the conical jet layers towards the center on one side and away from it on the other side. The latter is responsible for the creation of a helical, tubular structure that can be related to the observation of strong helical waves in the experiment (fig.4d in Liang and Max-
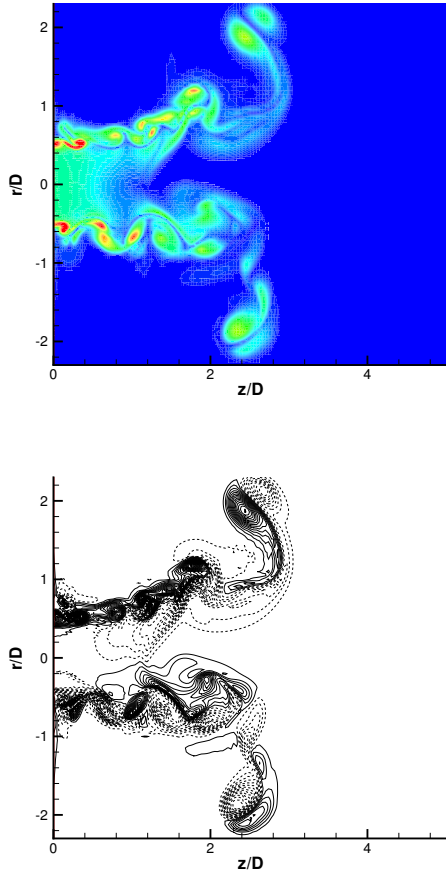
Figure 4: Enstrophy $|\mathbf{\Omega}|$ (upper graph, max $|\mathbf{\Omega}| = 16.97$, range shown is $[0, 12]$ with red indicating the highest value) and Ω_θ (lower graph, full lines are positive and dashed lines negative values) for $Re = 1000$ at $t = 12.96$ for the Liang and Maxworthy (2005) flow (case II).

worthy (2005) for a smaller swirl number $S = 0.9$). Liang and Maxworthy (2005) base their observation on flow visualisation using particle seeding, hence are their visualisations sets of streaklines. Since the flow is unsteady, streaklines are different from streamlines and pathlines and the relation of streaklines to enstrophy is not one-to-one since vorticity can be modified by stretching in contrast to passive scalars. There is no evidence of weak helical waves in the simulation (upper graph of fig.6), but the level surface of enstrophy (upper graph of fig.8) for the lower level value shows a helical tube wrapped around the conical jet.

The level surfaces of enstrophy in fig.8 indicate the presence of vortex reconnection. Weak vortex tubes are wrapped around the stronger tubes as is evident in the upper graph of fig.8, which is the precursor of viscous reconnection (see Shelley et al. (1993) for a thorough analysis).

CONCLUSIONS

The results show that the entrance profiles and the disturbances have a fundamental effect on the near field of the swirling jet flow.

The simulation of the Billant et al. (1998) flow (case I) shows that the entrance profile for v_z provides additional shear compared to the top hat profile. The formation of the
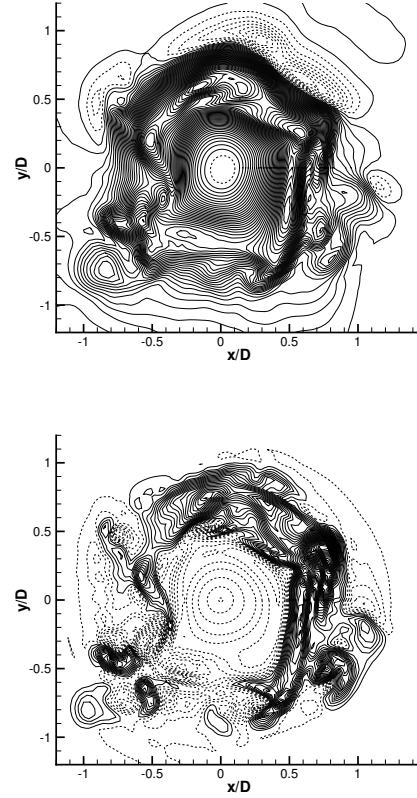

Figure 5: Axial velocity v_z (upper graph, full lines are positive and dashed lines negative values) and the vorticity mode combination $W = \Omega_\theta - iH(k)\Omega_r$ (lower graph) for $Re = 1000$, $S = 1.1$, $t = 12.96$ at the axial station $z/D = 1.22$ for the Liang and Maxworthy (2005) flow (case II).

recirculation zone is in the early phase dominated by vortex stretching near the axis and the appearance of three helical vortex tubes.

The simulation of the Liang-Maxworthy flow (2005) (case II), where the azimuthal velocity profile extends further into the boundary layer of the axial profile than for the Billant et al. (1998) case and disturbances near the entrace section are present, shows that the Rayleigh-Taylor instability of the cylindrical boundary layer $r/D = 0.4 \rightarrow 0.6$ forms longitudinal vortex tubes with a slowly increasing azimuthal angle. The effect of vortex stretching near the axis is less pronounced than for case I.

The simulation of the Liang-Maxworthy (2005) flow without the disturbances near the entrance section (case III) does not show the instability of the outer part of the conical shear layer as observed in case II. The azimuthal mode $k = 1$ becomes strong enough to generate a lateral motion that creates strong helical structures as evident in the experiment.

REFERENCES

Billant, P., Chomaz, J.M. and Huerre, P. (1998), "Experimental study of vortex breakdown in switling jets", JFM **376**, 183-219.

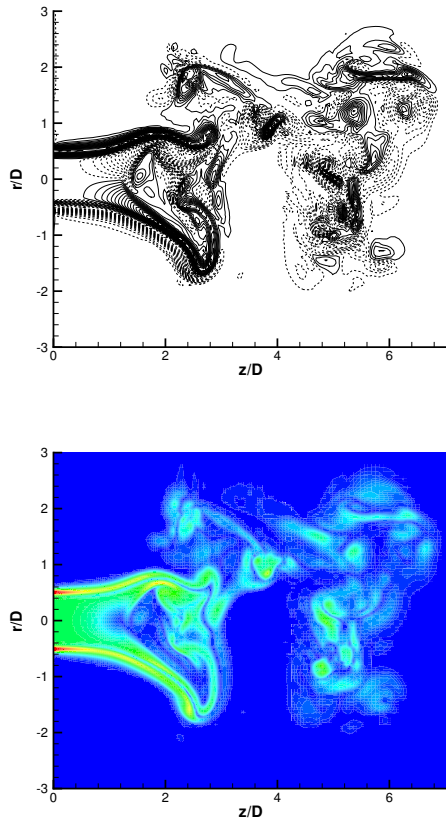Boyd, J.P. (2001), "Chebyshev and Fourier Spectral Methods", 2nd ed. Dover, Mineola.

Figure 6: Enstrophy $|\Omega|$ (lower graph, $\max|\Omega| = 11.85$, range shown is $[0, 10]$ with red indicating the highest value) and Ω_θ (upper graph, full lines are positive and dashed lines negative values) for $Re = 1000$, $S = 1.1$ at $t = 30.09$ for the Liang and Maxworthy (2005) flow (case III).
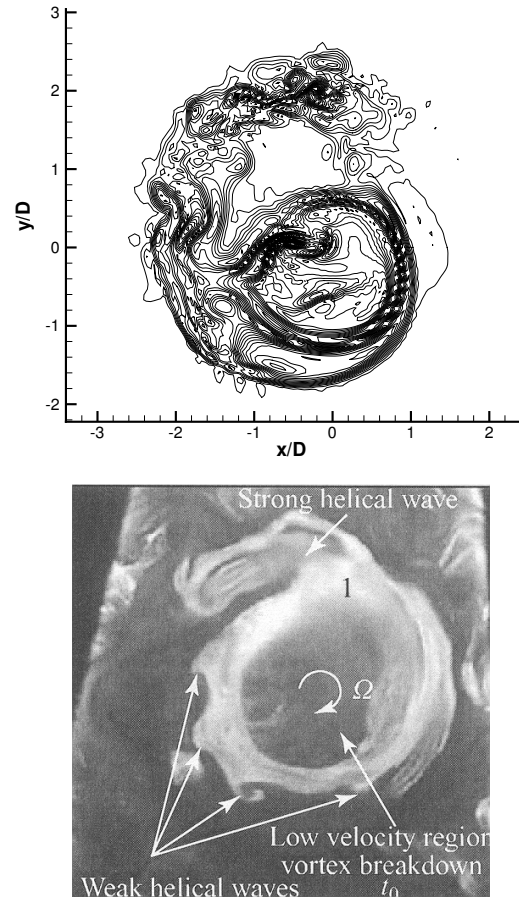

Figure 7: Instantaneous photo (fig.4d from Liang and Maxworthy (2005)) of horizontal jet slice for $Re = 1000$ and $S = 0.9$ at $z/D = 1.0$ (lower graph) and numerically simulated (case III) enstrophy section at $z/D = 2.38$, $t = 30.09$, $S = 1.1$, $Re = 1000$ (upper graph, opposite sense of rotation).

Constantinescu, G.S. and Lele, S.K. (2002), "A highly accurate technique for the treatment of flow equations at the polar axis in cylindrical coordinates using series expansions", J. Computat. Physics **183**, 165-186

Hairer, E. and Wanner, G. (1996), "Solving Ordinary Differential Equations II, Stiff and Differential-Algebraic Problems", 2nd ed., Springer Verlag Berlin.

Kollmann, W. and Roy, J.Y. (2000), "Hybrid Navier-Stokes solver in cylindrical coordinates I: Method", Computational Fluid Dynamics Journal **9**, 1-16.

Kollmann, W. (2007), "Simulation of vorticity dominated flows using a hybrid approach: I Formulation", to appear in Computers and Fluids.

Kurosaka, M., Cain, C.B., Srigrarom,S., Wimer, J.D., Dabiri, D., Johnson III, W.F., Hatcher, J.C., Thompson, B.R., Kikuchi, M., Hirano, K., Yuge, T., Honda, T. (2006), "Azimuthal vorticity gradient in the formative stages of vortex breakdown", JFM **569**, 1-28.

Leibovich, S. (1978), "The structure of vortex breakdown", Annual Rev. Fluid Mech. **10**, 221-246.

Liang, H. and Maxworthy, T. (2005), "An experimental investigation of swirling jets", JFM **525**, 115-159.

Ruith, M.R., Chen, P., Meiburg, E. and Maxworthy, T. (2003), "Three-dimensional vortex breakdown in swirling jets and wakes: direct numerical simulation", JFM **486**, 331-378.

Serre, E. and Bontoux, P. (2002), "Vortex breakdown in a three-dimensional swirling flow", JFM **459**, 347-370.

Shelley, M.J., Meiron, D.I. and Orszag, S.A. (1993), "Dynamical aspects of vortex reconnection of perturbed anti-parallel vortex tubes", JFM **246**, 613-652.
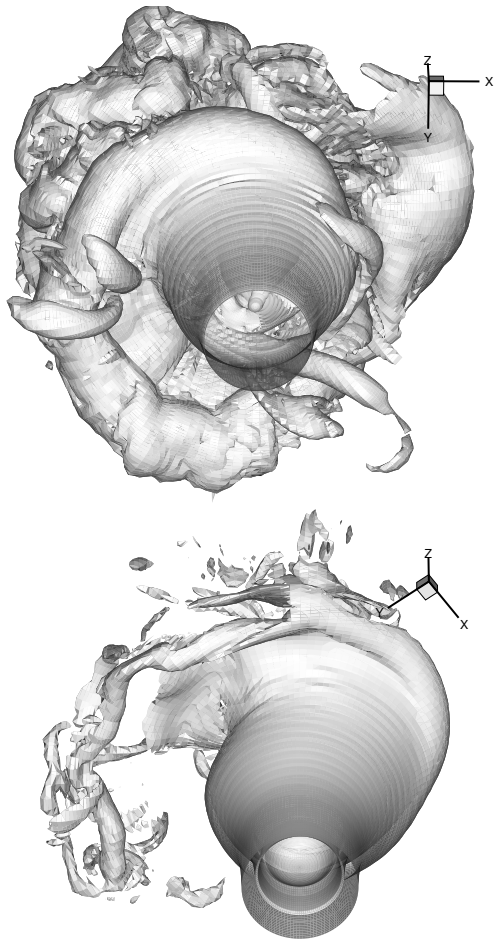
Figure 8: Level surfaces of enstrophy $e \equiv |\mathbf{\Omega}|$ (max $e = 17.54$) for two level values: upper graph $e = 0.8812$ and lower graph $e = 4.0538$ for $Re = 1000$, $S = 1.1$ at $t = 30.09$ for the Liang and Maxworthy (2005) flow (case III). The positive z-axis is the main flow direction.